JOURNAL OF GEOPHYSICAL RESEARCH, VOL. 114, C12006, doi:10.1029/2008JC005014, 2009

Lateral circulation and sediment transport driven by axial winds in an idealized, partially mixed estuary

Shih-Nan Chen,[1,2] Lawrence P. Sanford,[1] and David K. Ralston[3]

Received 11 July 2008; revised 17 August 2009; accepted 2 September 2009; published 3 December 2009.

[1] A 3D hydrodynamic model (ROMS) is used to investigate lateral circulation in a partially mixed estuary driven by axial wind events and to explore the associated transport of sediments. The channel is straight with a triangular cross section. The model results suggest that driving mechanisms for lateral circulation during axial wind events are different between stratified and unstratified conditions. When the water column is largely unstratified, rotational effects do not drive significant lateral circulation. Instead, differential advection of the axial salinity gradient by wind-driven axial flow is responsible for regulating the lateral salinity gradients that in turn drive bottom-divergent/convergent lateral circulation during down/up-estuary winds. From the subtidal lateral salt balance, it is found that the development of lateral salinity gradient by wind-induced differential advection is largely counterbalanced by the advection of salt by lateral circulation itself. When the water column is stratified, the lateral flow and salinity structures below the halocline closely resemble those driven by boundary mixing, and rotational effects are important. Lateral sediment flux and the event-integrated sediment transport are from channel to shoals during down-estuary winds but reversed for up-estuary winds. Potential impacts of wind-generated waves on lateral sediment transport are evaluated with two cases representing event conditions typical of upper Chesapeake Bay. Accounting for wind wave effects results in an order of magnitude increase in lateral sediment fluxes because of greater bottom stresses and sediment resuspension.

Citation: Chen, S.-N., L. P. Sanford, and D. K. Ralston (2009), Lateral circulation and sediment transport driven by axial winds in an idealized, partially mixed estuary, *J. Geophys. Res.*, *114*, C12006, doi:10.1029/2008JC005014.

1. Introduction

[2] Lateral circulation has long been recognized as an effective means to distribute scalars such as salt across estuaries [*Fischer et al.*, 1979]. It thus affects scalar dispersion rates, which set the residence time of a system and can potentially impact estuarine biogeochemical processes. Recently, redistribution of momentum by lateral circulation was also shown to contribute at the leading order to the subtidal, axial momentum balance [*Lerczak and Geyer*, 2004; *Huijts et al.*, 2008; *Scully et al.*, 2009]. Understanding the dynamics of lateral circulation is important to better comprehend how estuaries function.

[3] In previous examinations of the dynamics of lateral circulation, much attention has been placed on tidally forced processes. In the presence of tides, lateral circulation can be driven by interactions between barotropic tides with bathymetry [*Valle-Levinson et al.*, 2000], centrifugal acceleration in a curved, estuarine channel [*Chant and Wilson*, 1997; *Lacy and Monismith*, 2001], Ekman veering in the bottom boundary layer [*Ott and Garrett*, 1998], boundary mixing on a slope [*Chen and Sanford*, 2008], and differential advection of axial salinity gradients [*Nunes and Simpson*, 1985; *Lerczak and Geyer*, 2004]. Analytical models aiming to discern the relative importance of some of the above mechanisms have also been solved by prescribing the lateral density gradient [e.g., *Huijts et al.*, 2006].

[4] In comparison with active research on tidally forced processes, lateral circulation driven by wind forcing has received less attention. *Winant* [2004] and *Sanay and Valle-Levinson* [2005] investigated the wind-driven lateral circulation for homogeneous channels without tides. They found a major clockwise lateral circulation pattern (looking seaward; northern hemisphere) for a seaward directed wind consistent with Ekman dynamics. However, when salt is present, neither the wind-driven lateral circulation nor its interactions with tides are well studied.

[5] While Ekman dynamics are still expected to drive lateral circulation in the presence of salt, theoretically wind-driven axial circulation can provide another driving mechanism for lateral circulation. This mechanism is similar to the tidally induced differential advection. Key ingredients for differential advection mechanism are the presence of an axial salinity gradient and lateral shear in axial flow. For the pure tidally forced case, depth-averaged tidal currents tend

[1]Horn Point Laboratory, University of Maryland Center for Environmental Science, Cambridge, Maryland, USA.
[2]Now at Applied Ocean Physics and Engineering Department, Woods Hole Oceanographic Institution, Woods Hole, Massachusetts, USA.
[3]Applied Ocean Physics and Engineering Department, Woods Hole Oceanographic Institution, Woods Hole, Massachusetts, USA.

0148-0227/09/2008JC005014$09.00

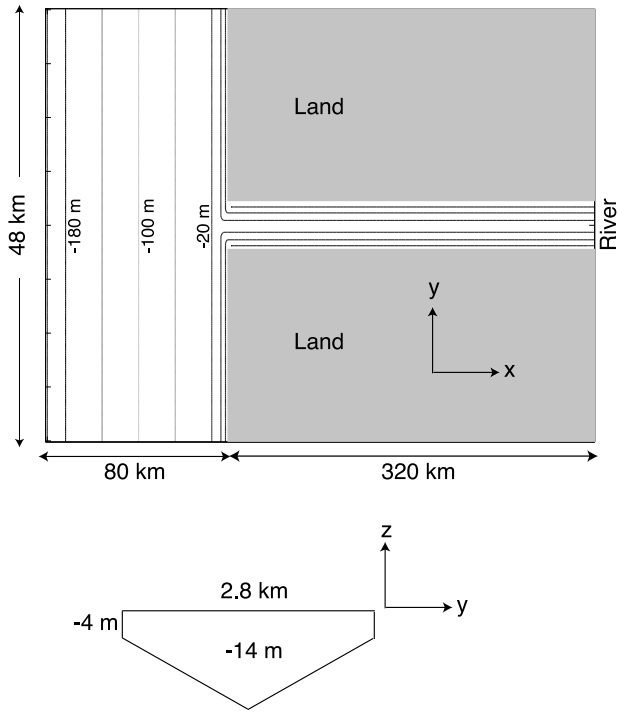

Figure 1. (top) Plan view of model domain and (bottom) the estuarine channel cross section. The domain mimics a broad continental shelf with a long, straight estuarine channel. The shelf size is 48 km (along shelf) × 80 km (cross shelf) with a constant slope from 200 m (off-shelf boundary) to 4 m (land boundary). The estuarine channel extends from x = 80 km to about 400 km. The gray areas are land. The channel is triangular shaped and of 2.8 km wide. The deep channel is 14 m, and the shallowest area is 4 m. Note that the domain is scaled disproportionately for better visualization.

to be stronger in the channel, which generates lateral shear. During floods, for example, this lateral shear then advects high salinity water further up estuary in the channel, creating a lateral baroclinic pressure gradient to drive lateral circulation [see *Lerczak and Geyer*, 2004]. Wind-driven axial flow over laterally varying bathymetry can also generate lateral shear. *Csanady* [1973] and *Wong* [1994] demonstrated that wind-driven flow is downwind on the shoal and upwind in the channel. Therefore, wind-induced lateral shear acting on an axial salinity gradient theoretically can create a lateral salinity gradient to drive lateral circulation.

[6] Lateral circulation can also transport suspended sediments across estuaries. This lateral transport integrated over time and combined with sedimentation may affect channel morphology. Although there has been an increasing amount of work on lateral sediment transport, the focus again has been again mainly on tidally forced processes [*Geyer et al.*, 1998; *Huijts et al.*, 2006; *Fugate et al.*, 2007; *Chen and Sanford*, 2008]. Lateral sediment transport during episodic wind events has been largely overlooked, even though in microtidal estuaries wind and tidal energy inputs can be comparable [*Zhong and Li*, 2006]. Taking Chesapeake Bay as an example, several field surveys have reported higher sedimentation rates in the channel, and the surficial sediment distribution shows a general pattern of muddy channel with sandy shoals [*Kerhin et al.*, 1988; *Colman et al.*, 1992]. Wind events with concurrent wind-generated wave action on shallow shoals have been hypothesized to transport fine-grain sediments across estuary and deposit them in the channel [*Langland and Cronin*, 2003]. However, this hypothesis has not yet been tested, and the lateral sediment transport associated with wind events has not been quantified.

[7] In this study, we carry out idealized numerical experiments to investigate lateral circulation and the associated transport of sediments during axial wind events. Our main focus is on the driving mechanism for lateral circulation when an axial salt gradient is present. In section 2, we briefly describe the model setup and the designs of numerical experiments. In section 3, we demonstrate that, when the stratification is weak, lateral salinity gradient is the primary driving force for lateral circulation during axial wind events, and the rotational effects (Ekman veering) are relatively weak. In addition, evidence is provided that wind-induced differential advection exerts an important control on the lateral salinity gradient. In section 4, we quantify the lateral sediment fluxes during wind events with different applied stresses. Two cases with wind wave forcing which represent typical event conditions in upper Chesapeake Bay are also included to evaluate the potential impacts of wind waves on lateral sediment transport. Finally, in section 5, the subtidal dynamics of lateral salinity gradients are evaluated with a salt balance equation, and a schematic diagram for wind-induced differential advection and its relationship with tides is presented.

2. Numerical Model

[8] We use the Regional Ocean Model System (ROMS) [*Haidvogel et al.*, 2000] to simulate an idealized estuarine channel. ROMS is a hydrostatic, primitive equation model using a curvilinear grid in the horizontal and a stretched, terrain-following coordinate in the vertical. It has been widely used by the coastal ocean modeling community and is capable of simulating many estuarine flows with high skill [e.g., *Warner et al.*, 2005; *Li et al.*, 2005]. The model domain consists of a straight estuarine channel and a wide inner shelf (Figure 1). The size of the shelf is 80 km across shelf × 48 km along shelf with a constant slope from 200 m at the offshore boundary to 4 m at the shoreline. A 2.8 km wide estuarine channel intersects the shelf and extends from x = 80 km to 400 km. The cross section is triangular shape with a maximum depth of 14 m in the channel and a minimum depth of 4 m on the sides. The lateral cross section is similar to, though slightly narrower than, upper Chesapeake Bay and the channel length is similar to Chesapeake Bay as a whole. The grid configuration is 194 (along channel, x direction) × 103 (cross channel, y direction) × 20 (vertical levels). The vertical levels are stretched with a lowest vertical resolution in the channel of 0.75 m. The estuary is highly resolved ($\Delta x \sim 2$ km, $\Delta y \sim 200$ m). Outside of this area, the grid is telescoped in the cross-channel direction ($\Delta y \sim 1.5$ km) to obtain a bigger salt pool on the shelf without increasing computational cost.

[9] Implementations of open boundary conditions and tidal forcing are described by *Chen and Sanford* [2008]. The resulting tide is largely progressive in the region with

Table 1. Wind Perturbation Experiments[a]

Experiment	τ_{wx} (Pa)	W	f (s^{-1})	H_s (m^{-1})
		Down-Estuary Wind		
0	0	0	0	0
1	−0.1	−0.85	0	0
3	−0.15	−1.27	0	0
5	−0.2	−1.79	0	0
7	−0.25	−2.11	0	0
9	−0.3	−2.53	0	0
11	−0.1	−0.80	10^{-4}	0
13	−0.3	−2.4	10^{-4}	0
15	−0.1	−0.85	0	1
		Up-Estuary Wind		
2	0.1	0.85	0	0
4	0.15	1.27	0	0
6	0.2	1.79	0	0
8	0.25	2.11	0	0
10	0.3	2.53	0	0
12	0.1	0.80	10^{-4}	0
14	0.3	2.4	10^{-4}	0
16	0.1	0.85	0	1

[a]Positive is up estuary. The event duration is 3 days (day 128 to 131). Here τ_{wx} is the wind stress, W is the Wedderburn number, f is the Coriolis parameter, and H_s is the wave height.

salt, and the depth-averaged tidal current amplitude is about 0.4 m s^{-1} in the middle of the estuary (half of the salt intrusion). A constant river flow of 0.01 m s^{-1} is imposed at the river end. The $k-\varepsilon$ turbulence closure [*Jones and Launder*, 1972] is activated with a stability function proposed by *Canuto et al.* [2001]. *Chen and Sanford* [2008] applied a nearly identical model setup to investigate tidally driven lateral circulation and found that both flow and salinity fields are insensitive to the choice of closures among $k-\varepsilon$, $k-\omega$, and MY2.5. The salinity field reaches a steady structure modulated by semidiurnal tides in 120 days.

[10] We incorporate a single layer, single grain size sediment bed to explore lateral sediment transport. The sediment bed is sufficiently thick so that sediment is never depleted. The erosion formulation is the Ariathurai-Partheniades type, and the deposition is continuous with a constant settling speed of 0.3 mm s^{-1}. Details of the sediment transport module can be found in the work of *Chen and Sanford* [2008]. Without surface gravity waves, bottom stress is computed by assuming a logarithmic current profile in the lowest computational cell and a constant bottom roughness parameter (z_0) of 0.5 mm. With surface gravity waves, a maximum combined wave-current bottom stress is computed using *Madsen*'s [1994] formulations with prescribed wave height, period, angle, and the same z_0 for consistency. The wave number is approximated by using the 6th-degree polynomial by *Dean and Dalrymple* [1991].

[11] After the salt structure reaches a steady state, we then perform numerical experiments (Table 1) to investigate the dynamics of lateral circulation driven by axial wind and the associated transport of sediments. Following *Chen and Sanford* [2009], we design the experiments based on a nondimensional number, the Wedderburn number (W). The Wedderburn number is the ratio of the vertical gradient of the wind stress to the baroclinic pressure gradient force [*Monismith*, 1986]

$$W = \frac{\tau_{wx} L}{\Delta\rho g H^2}, \tag{1}$$

where τ_{wx} is the axial wind stress (positive is up estuary), L is the length of the estuary, $\Delta\rho$ is the density change over L, g is the gravitational acceleration, and H is the averaged depth. W thus indicates the relative strength of wind-driven and gravitational circulations on subtidal axial flows [*Geyer*, 1997]. For example, when $|W| > 1$, wind-driven circulation is expected to have significant influences on the cross-sectional structures of subtidal axial flows and therefore the subtidal salinity field.

[12] We consider the results of 17 numerical experiments (Table 1) in this paper. The baseline case (number 0) is the simplest possible condition: no wind, no Coriolis acceleration, and no waves. In the 16 wind perturbation experiments, we change wind magnitude, direction and turn on/off Coriolis acceleration and wave forcing while keeping the duration of wind event constant (3 days). The wind direction is either up estuary (positive) or down estuary (negative). The wind stresses range from 0.1 to 0.3 Pa, bracketing $|W|$ from about unity to 2.5. Conditions with $|W| \ll 1$ are not considered here because *Chen and Sanford* [2009] found that such weak wind stresses have minor effects on stratification and subtidal velocity/salinity fields. A wind stress of 0.1 Pa (∼wind speed of 8 m s^{-1} based on *Large and Pond* [1981]) represents a typical moderate event condition in Chesapeake Bay [*Lin et al.*, 2002]. Wind is ramped up and down 5 h before the event onset and end, respectively. Wind stress is constant from 5 h after day 128 to 5 h before day 131. Case numbers 15 and 16 account for the influences of wind-generated waves. Two empirical formulas are used to estimate fetch-limited wind waves [*Resio et al.*, 2002; *Goda*, 2003]. Approximating fetch by the distance from the mouth to the middle of the estuary where we evaluate lateral dynamics, both formulas yield similar estimates of 1 m wave height (H_s) and 3.5 s wave period (T_s). These estimates are consistent with observed typical values in Chesapeake Bay [*Lin et al.*, 2002] and are used to derive the combined wave-current bottom stress in the sediment transport component.

[13] The model simulates a partially mixed estuary. The length of the estuary, defined by the distance between 2 and 30 psu tidally averaged isohalines in the channel, is about 145 km. At the middle of estuary (denoted by a vertical line in Figure 2a), the tidally averaged top-bottom salinity difference is 4.5 psu. The vertical profile of tidally averaged, along-channel velocity in the channel (Figure 2b) is as expected consistent with gravitational circulation, with a landward flow near bottom and a seaward flow near surface. In cross section (Figures 2c and 2d), the isohalines are mostly horizontal in the interior but intersect the bottom slope at a right angle, and the near-bottom lateral flows are up slope at both maximum ebb and flood. These patterns are consistent with the lateral circulation driven by boundary mixing on a slope [*Chen and Sanford*, 2008]. Bottom stress shows flood-ebb asymmetry due to the presence of gravitational circulation (Figure 2e). Detailed lateral dynamics for the baseline case are described by *Chen and Sanford* [2008].

3. Dynamics of Lateral Circulation During Wind Events

3.1. Cross-Sectional Structures of Flow and Salinity Field at Different Tidal Phases

[14] To examine the dynamics of lateral circulation during wind events, we contrast two representative wind-forcing

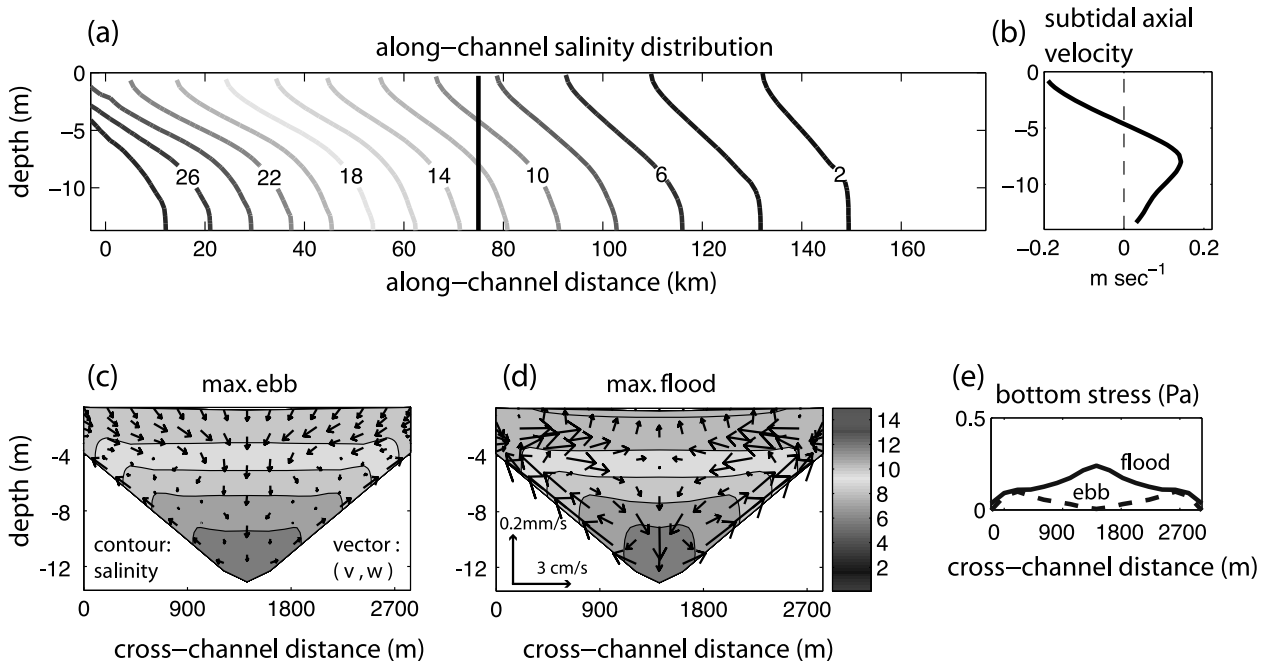

Figure 2. (a) Along-channel salt structure, (b) vertical profile of subtidal axial velocity, cross-sectional structures of salinity (color contour) and lateral circulation (vectors) at maximum (c) ebb and (d) flood, and (e) lateral distribution of bottom shear stress at maximum flood (solid curve) and ebb (dashed curve) for the baseline case (number 0 in Table 1). Slices in Figures 2b–2e are taken at the channel midpoint indicated by the vertical line in Figure 2a. The channel midpoint defined as half of the salt intrusion length (∼145 km).

regimes and begin with the simplest condition without rotation. In cases 1 and 2 (moderate winds) wind-driven axial circulation is comparable to gravitational circulation (Figure 3), whereas in cases 9 and 10 (strong winds) wind-driven flow dominates (Figure 4). These two regimes also provide contrasting behaviors in stratification. For moderate wind, the wind-induced straining of the along-estuary salinity field exerts important controls on stratification, leading to enhanced stratification during down-estuary wind but destratification during up-estuary wind [*Scully et al.*, 2005; *Chen and Sanford*, 2009]. For strong wind, on the other hand, the wind stress is large enough to mix the water column [*Chen and Sanford*, 2009]. These wind effects on stratification have profound influences on lateral circulation.

[15] The general wind responses consist of a transient adjustment period at the beginning of the event when sea level is set up or down, a quasi-steady period during the event, and another transient adjustment after the event. The adjustment period is about 1.5 day (day 128–129.5 and 131–132.5), with a shorter adjustment period and more well-defined quasi-steady period during strong winds (see section 5.3 for discussion). Cross-sectional profiles described below are taken during the quasi-steady period (day 129.875, 130, and 130.125 for maximum. ebb, slack, and maximum. flood, respectively).

[16] During moderate down-estuary wind, the water column stays stratified. Below the halocline at around 6 m, the up-slope directed, near-bottom lateral flows and the flat interior isohalines tilted normal to the slope at different tidal phases (Figures 3a–3c) are similar to the baseline case (Figure 2), suggesting that boundary mixing still drives a significant amount of lateral circulation. Above the halocline (i.e., surface mixed layer), the lateral circulation pattern is more complex. Two circulation cells symmetric about the channel axis are present during most tidal phases. Lateral flow converges at the surface in the center of the channel and diverges just above the halocline. Salinity is vertically uniform in this layer. Salinity in the center of the channel axis is persistently higher than that on the shoals. The resulting baroclinic pressure gradients increase with depth and drive the two circulation cells. Maximum lateral flows do not change significantly over a tidal cycle, ranging from 2.0 to 2.3 cm s^{-1}. Axial velocity is strongly sheared near surface during maximum ebb (Figure 3a) and shows a strong subsurface maximum during maximum flood (Figure 3c) because wind-driven circulation reinforces gravitational circulation (see section 3.4).

[17] During moderate up-estuary wind, the water column is unstratified. Two symmetrical circulation cells converging near the bottom of the channel are apparent throughout the tidal phases (Figures 3d–3f). The lateral salinity gradients are reversed with slightly higher salinity on the shoals, which then drive the bottom-convergent lateral circulation. Lateral flows here are stronger than those during moderate down-estuary wind. Maximum lateral flows do not change much over a tidal cycle, ranging from 4.3 to 4.8 cm s^{-1}. The vertical shear in the axial velocity is reduced in comparison to the moderate down-estuary wind case because wind-driven axial flow nearly cancels the gravitational circulation.

[18] In contrast to the stratified condition during moderate down-estuary wind, the water column is largely unstratified during strong down-estuary wind (Figures 4a–4c). The lateral circulation pattern that was previously confined to

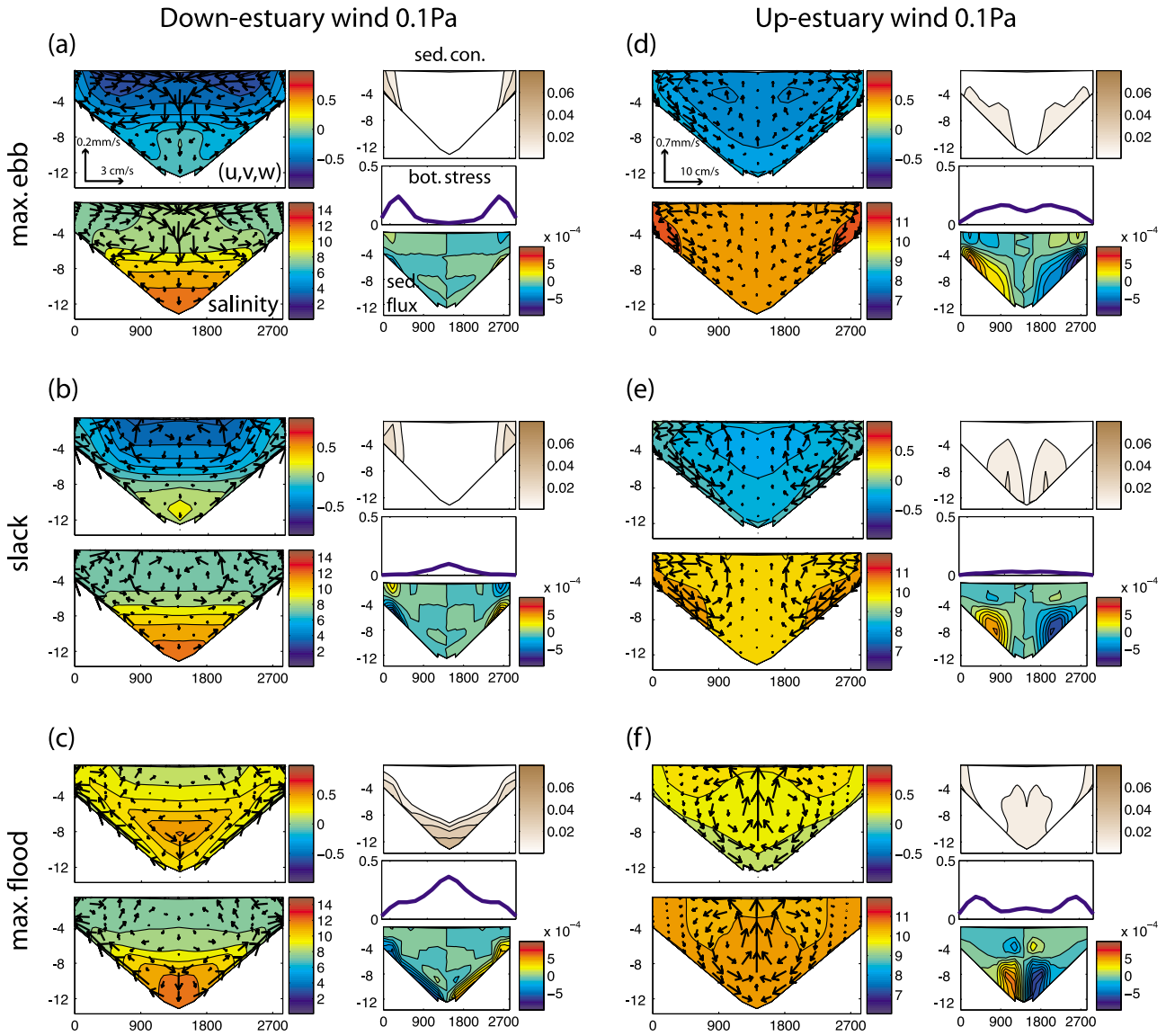

Figure 3. Cross-sectional structures (looking seaward) of five variables for the moderate (a–c) down-estuary and (d–f) up-estuary wind cases (numbers 1 and 2 in Table 1). The profiles are taken at maximum ebb (Figures 3a and 3d), around slack (Figures 3b and 3e), and at maximum flood (Figures 3c and 3f). The subplots in Figures 3a–3f are as follows: The top left is velocity field (u, v, w); negative values in the color bar represent ebbs. The bottom left is salinity and (v, w). The top right is suspended sediment concentration (kg m^{-3}). The middle right is bottom stress (Pa). The bottom right is lateral sediment flux (kg m^{-2} s^{-1}); positive values in the color bar represent transport toward the right. Again the slices are taken at the channel midpoint (fixed location denoted by the vertical line in Figure 2a).

the surface layer now penetrates the entire water column. Salinity at the center is persistently higher than that on the shoals, setting up a baroclinic pressure gradient force that drives a bottom-divergent lateral circulation. While the bottom-divergent pattern persists at different tidal phases, its magnitude increases from 2.5 cm s^{-1} at maximum ebb (Figure 4a) to 4.8 cm s^{-1} at maximum flood (Figure 4c).

[19] Cross-sectional structures of flow and salinity fields during strong up-estuary wind (Figures 4d–4f) are similar to those during moderate up-estuary wind (Figures 3d–3f) but with larger magnitudes. The lateral circulation features two symmetric circulation cells that converge near the bottom. Salinity on the shoals is persistently higher than that in the channel, reversing the lateral salinity gradient and thus driving near-bottom lateral flows toward the channel. The magnitude of lateral flow displays considerable tidal variation. Maximum lateral flow decreases from 11.0 cm s^{-1} at maximum ebb to 5.1 cm s^{-1} at maximum flood, which is opposite to the increasing trend from ebb to flood during strong down-estuary wind. It should be noted that the cross-sectionally averaged salinity is higher during up-estuary winds (e.g., comparing Figures 4c and 4f). This is because sea level adjustment at the onset of up-estuary winds drives transient up-estuary salt fluxes that increase the length of salt intrusion [*Chen and Sanford*, 2009]. The lateral circulation patterns described above are however not

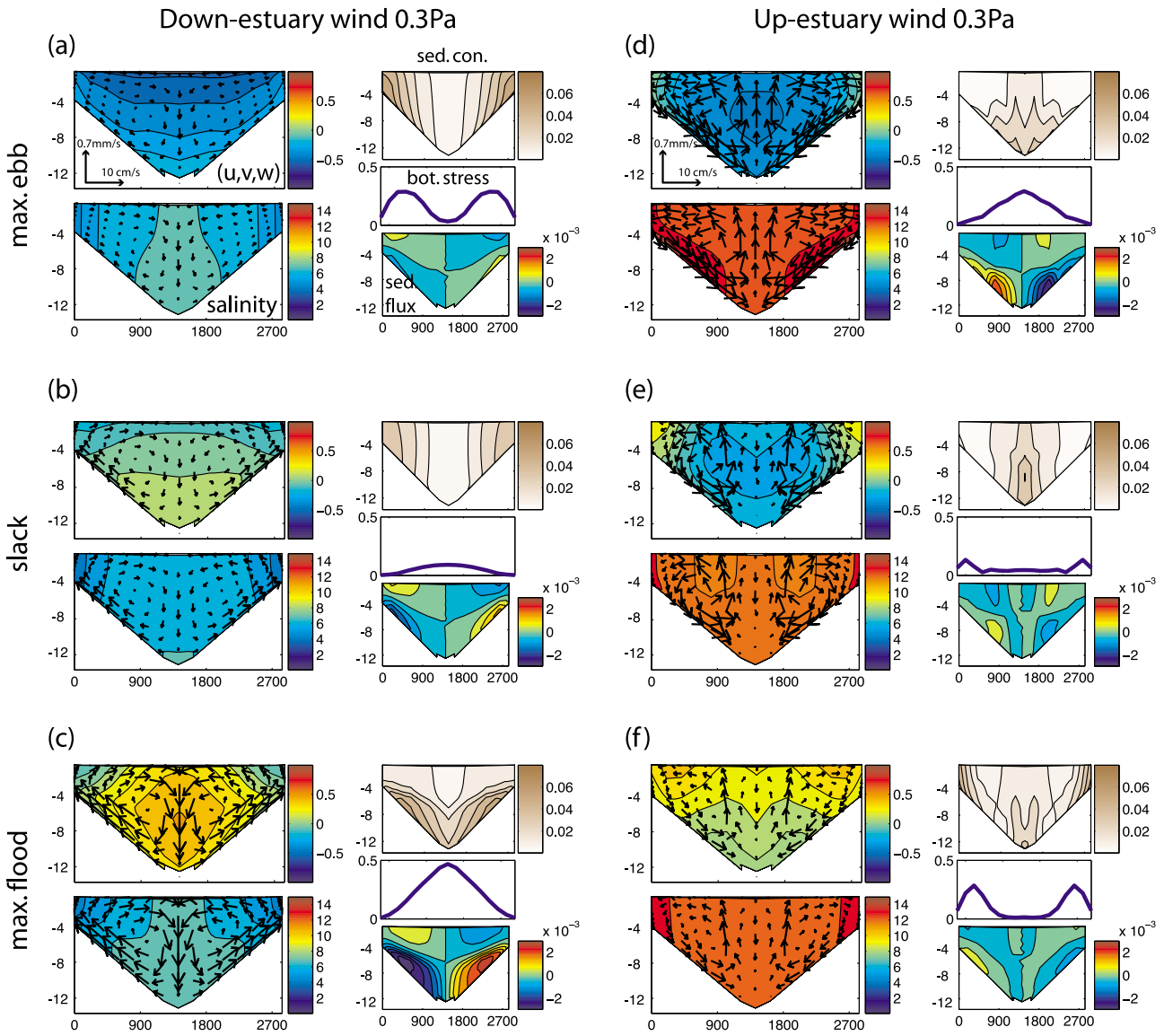

Figure 4. Same as Figure 3 but for the strong (a–c) down-estuary and (d–f) up-estuary wind cases (numbers 9 and 10 in Table 1).

sensitive to the location of the lateral slice as long as the slice is a tidal excursion away from the salt nose.

3.2. Momentum Budget in the Cross-Channel Direction

[20] Next we look at the momentum balance in the cross-channel direction. Each momentum term in equation (2) is averaged over the lower left half (looking seaward; within 4.5 mab) of the water column because both the lateral flow and pressure gradient force change signs in the vertical

$$v_t + \left(uv_x + vv_y + wv_z\right) = -P_y/\rho_0 + \left(A_v v_z\right)_z. \qquad (2)$$

It is clear that the main balance is between lateral pressure gradient force (P_y/ρ_0) and vertical stress divergence ($(A_v v_z)_z$) in all four cases, although the contribution from unsteadiness (v_t) and nonlinear advection ($uv_x + vv_y + wv_z$) can't be ignored at times for up-estuary wind cases (Figure 5). The dominance of P_y/ρ_0 confirms that the lateral pressure gradient is the driving force for lateral circulation.

[21] Axial wind appears to be the primary forcing generating the lateral pressure gradient (Figure 5). During down-estuary winds, P_y/ρ_0 is enhanced, especially when the wind stress is strong (Figure 5b), and the magnitude of the pressure gradient is larger during floods (e.g., 2nd vertical line). During up-estuary winds, P_y/ρ_0 changes sign, which is consistent with the persistently saltier shoal in Figures 3d–3f and 4d–4f. The pressure gradient has the opposite tidal variation from the down-estuary wind cases, showing larger magnitude during ebbs (e.g., 1st vertical line) (see section 5.2).

3.3. Lateral Salinity Gradient and Lateral Flows

[22] The pressure gradient-stress divergence balance in the momentum budget is reminiscent of the classic theory of estuarine circulation by *Hansen and Rattray* [1965] but in the lateral direction [*Nunes and Simpson*, 1985]. Since the

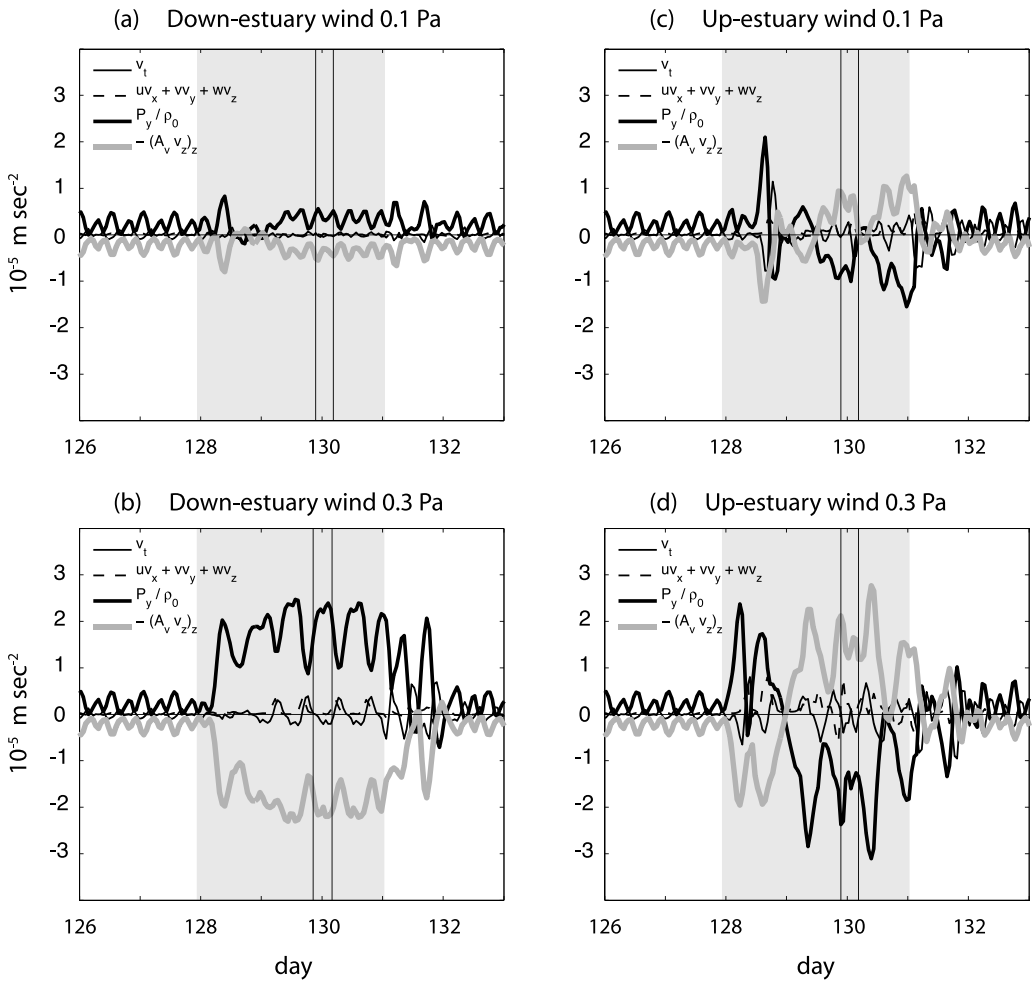

Figure 5. Time series of lateral momentum budget for (a) moderate down-estuary wind, (b) strong down-estuary wind, (c) moderate up-estuary wind, and (d) strong up-estuary wind cases. Each momentum term is averaged over the lower left half of the cross section in Figure 3. There are two vertical lines. They correspond to maximum ebb and maximum flood when the cross-sectional profiles in Figures 3 and 4 are taken. The gray shading represents the event period.

wind forcing is strictly axial and the Coriolis acceleration is turned off (this will be relaxed in section 3.5), the pressure gradient is dominated by baroclinicity. Hence, the pressure gradient-stress divergence balance implies that lateral salinity gradient ($\partial s/\partial y$) drives lateral circulation. To examine such relationship, the time series of lateral flow is overlaid with $\partial s/\partial y$ in Figure 6. The time series is taken at the midpoint on the left slope (y = 700 m in Figures 3 and 4), and $\partial s/\partial y$ is computed by differencing the salinity between two nearest grid points (y = 500 and 900 m; z is constant). A positive value means the channel region is saltier. The computed $\partial s/\partial y$ is fairly uniform in the vertical in three unstratified cases (Figures 6b–6d), so we depth average for a representative value. Lateral flow is only averaged over the bottom half (to 4.5 mab) of the water column because lateral flow largely cancels out when integrating over the whole water column.

[23] As expected, lateral flow (v) is correlated with $\partial s/\partial y$ in the three unstratified cases (Figures 6b–6d). The correlation coefficients are 0.56, 0.76, and 0.81 for strong down-estuary, moderate up-estuary, and strong up-estuary cases, respectively. Wind modifications on $\partial s/\partial y$ and lateral flow are also coherent with the variations in P_y/ρ_0 and the vertical stress divergence in the momentum budget. During strong down-estuary wind, $\partial s/\partial y$ is enhanced and stays positive, which then drives stronger bottom-divergent flows. During up-estuary winds, $\partial s/\partial y$ is reversed and stays negative after the initial response (around day 129.5). The negative $\partial s/\partial y$ then drives bottom-convergent flows. For the moderate down-estuary wind case in which the water column is stratified, lateral flows are weaker ($\sim$0.015 m s^{-1}) and $\partial s/\partial y$ doesn't change much. Moreover, $\partial s/\partial y$ and v are less correlated (correlation coefficient is 0.29), in part because $\partial s/\partial y$ has more vertical structures than the unstratified cases. We correlate the near-bottom $\partial s/\partial y$ with v and improve the correlation (0.57). This implies that bottom boundary layer processes may play a significant role in driving lateral flows in stratified conditions (e.g., Figures 3a–3c).

3.4. Wind Modifications of Lateral Shear in Axial Velocity and Lateral Salinity Gradient

[24] Results from the previous sections demonstrate that, when the water column is unstratified, $\partial s/\partial y$ shows large wind modulations, with salinity on the shoals persistently

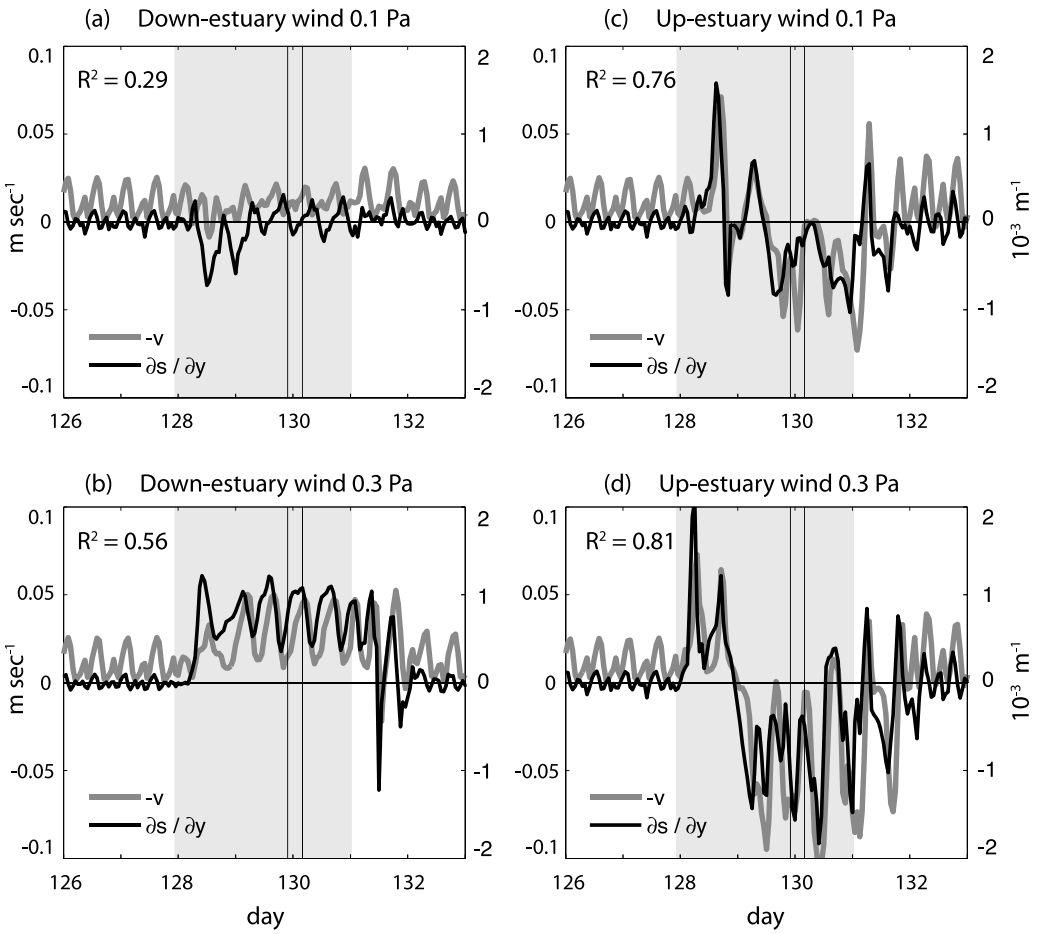

Figure 6. Time series of lateral salinity gradient ($\partial s/\partial y$; black curves) and lateral flow ($-v$; dark gray curves) for (a) moderate down-estuary wind, (b) strong down-estuary wind, (c) moderate up-estuary wind, and (d) strong up-estuary wind cases. The time series is taken at the midpoint on the left slope (e.g., y = 700 m in Figure 3). Here $\partial s/\partial y$ is computed by differencing the salinity between two nearest grid points (y = 500 and 900 m; constant z) and then depth averaged. A positive value means the channel region is saltier. Lateral flow is only averaged over the bottom half of the water column (within 4.5 mab). On this half of the cross section, positive v means flow is from shoal to channel. The two vertical lines indicate maximum ebb and maximum flood. The gray shading represents the event period.

higher/lower than in the channel during up/down-estuary wind, which then leads to a bottom-convergent/divergent lateral circulation pattern. The persistent salinity gradient over a tidal cycle is inconsistent with the gradient reversal ($\partial s/\partial y$ change sign) between flood and ebb expected from the pure tidally driven differential advection mechanism [*Nunes and Simpson*, 1985; *Lerczak and Geyer*, 2004]. The inconsistency thus implies wind modifications of lateral shear.

[25] To examine the wind influences on lateral shear, we first look at the cross-sectional structures of subtidal (33 h low-pass filtered) axial velocity (Figure 7). In a channel with a triangular cross section, we expect subtidal axial flow to show considerable lateral variations during wind events because pure wind-driven flow is downwind on the shoals and upwind in the channel [*Csanady*, 1973; *Wong*, 1994; *Sanay and Valle-Levinson*, 2005]. Without wind, the subtidal axial flow at the channel midpoint is primarily vertically segregated, consistent with gravitational circulation (Figure 7a). In general, down-estuary wind enhances the magnitude of subtidal flow because wind-driven flow and gravitational circulation are in concert (Figures 7b and 7c). The subtidal flow during moderate down-estuary wind shows small lateral variations because stratification limits vertical momentum exchange, allowing the subtidal flow to remain vertically segregated [e.g., *Guo and Valle-Levinson*, 2008]. However, the subtidal flow indeed shows large lateral variations during strong down-estuary wind (Figure 7c). The subtidal flow becomes more laterally segregated when wind-driven axial flow dominates ($W \sim -2.5$) and the water column is unstratified. This enhanced subtidal lateral shear could then advect the salinity gradient further down estuary on the shoals and up estuary in the channel. This laterally sheared advection could withstand the tendency of reversing gradient during ebbs, which then leads to a persistently saltier channel region.

[26] Moderate and strong up-estuary winds reverse the subtidal lateral shear. During moderate wind, the subtidal axial flow is weak because wind-driven flow nearly cancels gravitational circulation ($W \sim 0.85$; Figure 7d). However,

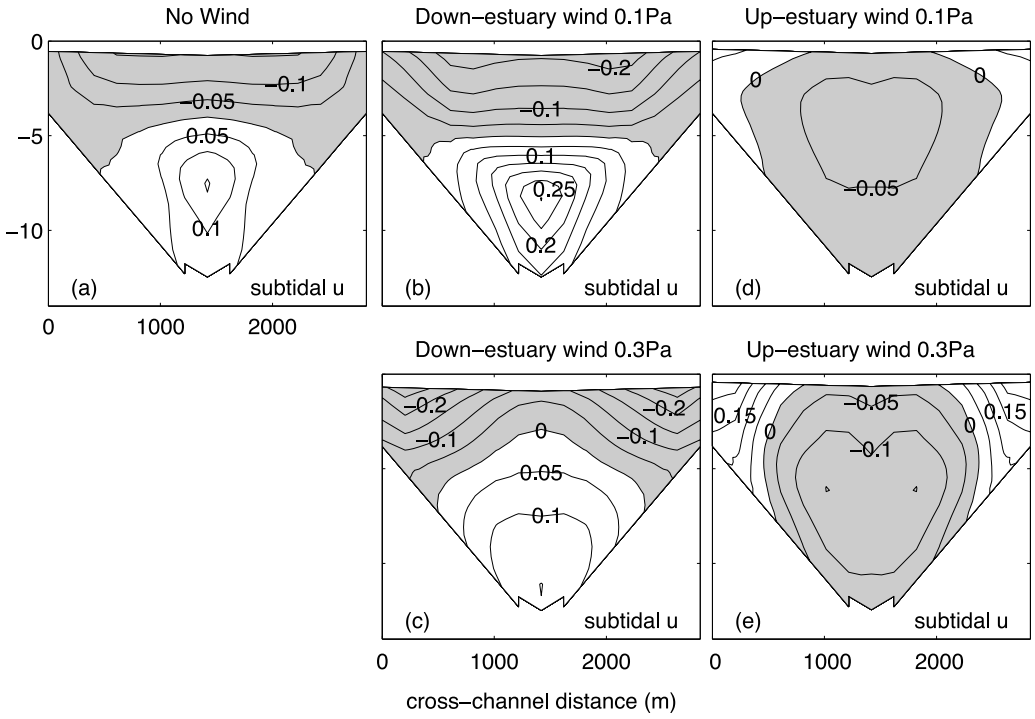

Figure 7. Cross-sectional structures of subtidal axial velocity at the channel midpoint at day 130. The (a) no wind, (b) moderate down-estuary wind, (c) strong down-estuary wind, (d) moderate up-estuary wind, and (e) strong up-estuary wind cases are shown. The gray shading indicates down estuary (negative).

the subtidal flow is up estuary on the shoals and down estuary in the channel, revealing the wind influence. As the wind-driven flow dominates during strong wind, reversal of the subtidal lateral shear becomes apparent ($W \sim 2.5$; Figure 7e). The reversed, laterally sheared flow then advects salt further up estuary on the shoals and down estuary in the channel to create shoal regions with persistently higher salinity, as shown in Figures 3d–3f and 4d–4f.

[27] Time series comparisons support the conclusion that wind modification of lateral shear is responsible for the changes in the lateral salinity gradient. Lateral shear ($\partial u/\partial y$) is computed at the midpoint on the left slope and then depth averaged, as for $\partial s/\partial y$ in section 3.3. A positive value means that the axial velocity increases (becomes less negative) toward the channel center. In general, changes in subtidal lateral shear correspond to the changes in $\partial s/\partial y$. During strong down-estuary wind, lateral shear and $\partial s/\partial y$ both increase (Figures 8c and 8d), whereas during up-estuary winds lateral shear and $\partial s/\partial y$ both change sign and decrease (Figures 8e–8h). Stronger wind stress leads to larger changes. However, when the water column is stratified, wind modifications of lateral shear and $\partial s/\partial y$ are minor, except during the transient periods (Figures 8a and 8b).

[28] Strong transient effects due to seal level adjustment are apparent within about 1.5 day after the event onset [*Chen and Sanford*, 2009]. For example, at the beginning of a down-estuary wind event, sea level starts to tilt down toward the head of the estuary accompanying net down-estuary volume transport. This transient down-estuary flow is stronger in the channel and hence temporarily reduces or reverses lateral shear (Figures 8a and 8c after day 128).

3.5. Influences of Earth's Rotation

[29] Including Earth's rotation induces axial asymmetry in lateral circulation, but, when the water column is unstratified, the lateral circulation patterns are similar to those without rotation. During strong down/up-estuary wind, both nonrotating and rotating cases show a pattern of two lateral circulation cells with flow divergence/convergence near the bottom (Figures 9c, 9d, 9g, and 9h). The circulation cells in the rotating cases are slightly asymmetrical about the channel axis (Figures 9d and 9h). Similar results are found during moderate up-estuary wind. The bottom-convergent lateral circulation can still be seen when rotation is included (Figure 9f), but the right side of the cell is stronger than the left side (looking seaward) and the axial asymmetry in lateral circulation is larger than the strong wind cases.

[30] The similarity in lateral circulation patterns between nonrotating and rotating cases breaks down when the water column is stratified. During moderate down-estuary wind, the lateral circulation with rotation is radically different from that without rotation (Figures 9a and 9b). With rotation, the lateral circulation during flood tide is dominated by a counterclockwise circulation consistent with baroclinic relaxation of the upwelled salt structure reinforced by Ekman veering in the bottom boundary layer. The pattern reverses strongly on ebb tide as the wind and tide work in concert. The lateral internal seiche response of the estuary [*Sanford et al.*, 1990] may also play a role. This circulation pattern is interesting, but highly complex; its full exploration is beyond the scope of the present paper.

[31] We further explore comparisons between the magnitudes and temporal variations of lateral flows with and

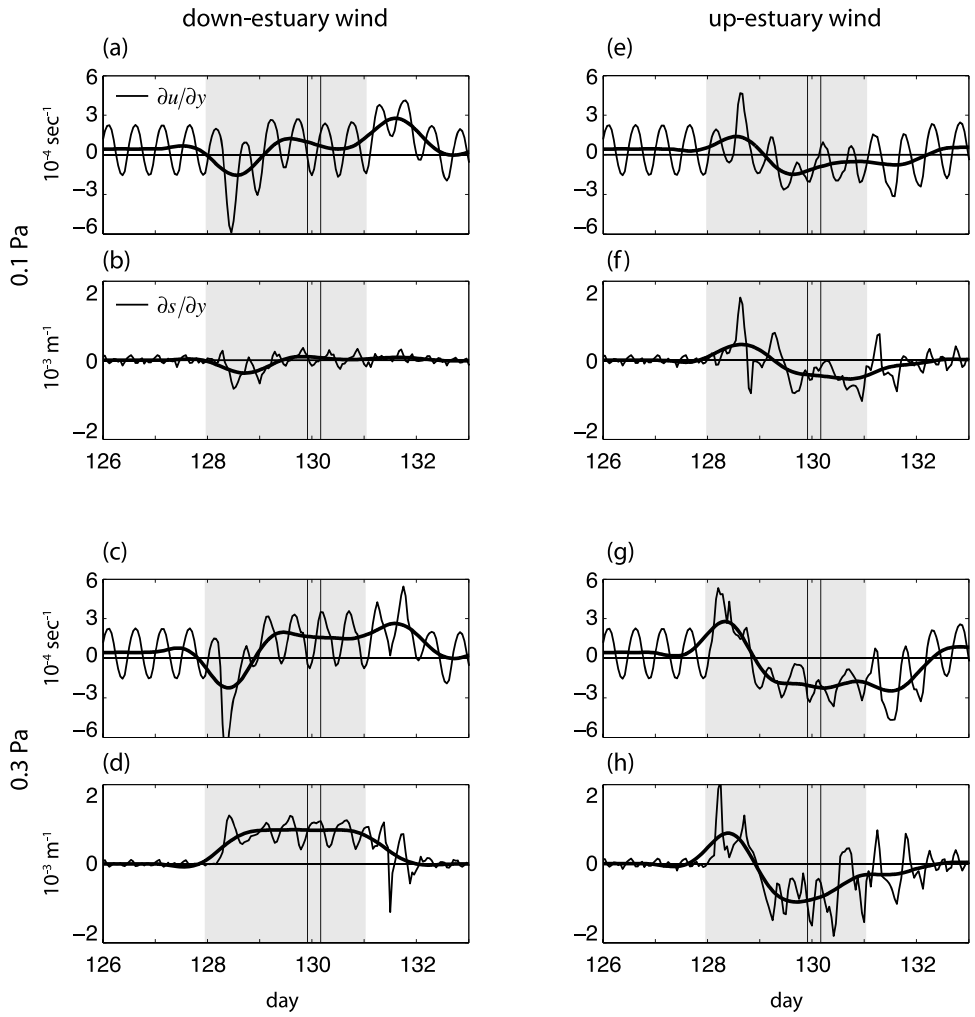

Figure 8. Time series comparisons between (a, c, e, and g) lateral shear in axial velocity ($\partial u/\partial y$) and (b, d, f, and h) lateral salinity gradient ($\partial s/\partial y$). The time series is taken at the midpoint on the left slope. Here $\partial u/\partial y$ is computed in the same way as $\partial s/\partial y$ in Figure 6. A positive $\partial u/\partial y$ means axial flow velocity increases toward the channel. Figures 8a–8d and Figures 8e–8h are down-estuary and up-estuary wind, respectively. Figures 8a, 8b, 8e, and 8f are with moderate wind, whereas Figures 8c, 8d, 8g, and 8h are with strong wind. The two vertical lines indicate maximum ebb and maximum flood. The thick curve represents the subtidal signal (33 h low-pass filtered). The gray shading represents the event period.

without rotation. The strength of lateral flow is characterized by the cross-sectionally averaged lateral velocity magnitude ($\overline{v}$)

$$\overline{v} = \frac{1}{A}\int |v| \cdot dA. \tag{3}$$

During strong winds, the time series of lateral flow with/without rotation are nearly identical, especially after the transient adjustment (day 129–131 in Figures 10b and 10d). The correlation coefficients are 0.88 and 0.86 for strong down- and up-estuary wind, respectively. During moderate up-estuary wind, the lateral flow magnitude with rotation is 49% higher than that without rotation (event averaged), and the correlation coefficient diminishes slightly to 0.66 (Figure 10c). Again, the similarity between nonrotating and rotating cases breaks down under stratified conditions. During moderate down-estuary wind, the lateral flow magnitude with rotation is 82% higher than that without rotation (event averaged), and the correlation coefficient is low with a value of 0.28 (Figure 10a).

4. Lateral Sediment Transport

4.1. Patterns of Lateral Sediment Transport at Different Tidal Phases

[32] We begin our exploration of lateral sediment transport by examining the cross-channel distribution of bottom shear stress that mobilizes the sediments. The interactions between tidal currents, wind-driven flow, and gravitational circulation control the bottom stress distribution which varies with wind direction and exhibits considerable tidal variations. During down-estuary winds, bottom stress peaks in the channel during flood when the flooding currents, wind-driven circulation, and gravitational circulation are all

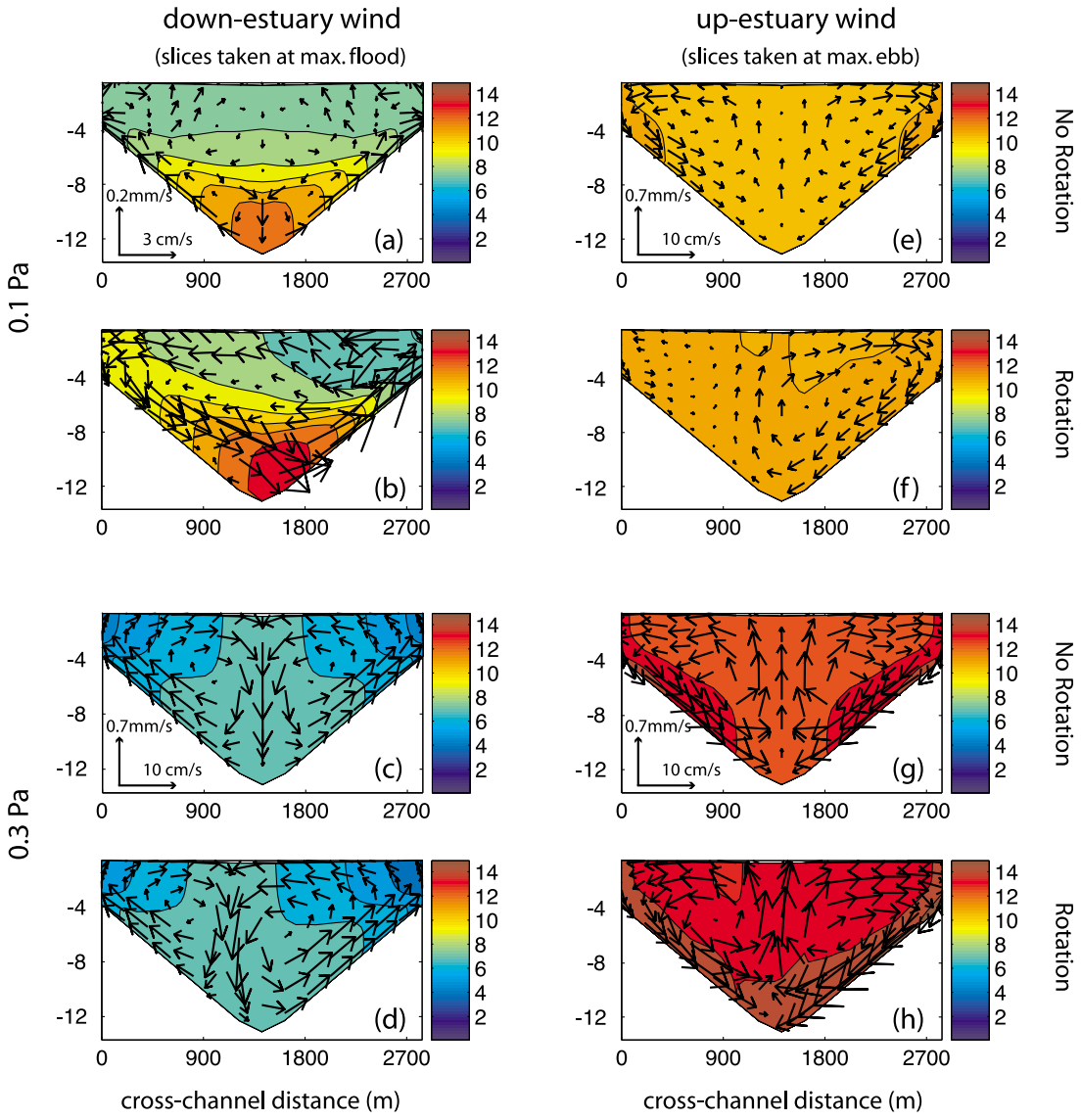

Figure 9. Comparisons of the cross-sectional structures of salinity (color contour) and lateral circulation (vectors) between the cases (a, c, e, and g) without rotation and (b, d, f, and h) with rotation. Figures 9a–9d are for down-estuary wind, and the profiles are taken at maximum flood. Figures 9e–9h are for up-estuary wind, and the profiles are taken at maximum ebb. Figures 9a, 9b, 9e, and 9f are with moderate wind forcing, whereas the Figures 9c, 9d, 9g, and 9h are with strong wind forcing. Note that the vector scale for the moderate down-estuary wind case is exaggerated 4 times relative to the rest of the cases.

directed up estuary in the channel (Figures 3c and 4c). As expected, bottom stress is weak at slack, but there is still a small peak in the channel (Figures 3b and 4b) because the presence of down-estuary wind strengthens the subtidal axial velocity (Figures 5b and 5c; section 3.2). At ebbs, the peak of bottom stress in the channel disappears because ebbing currents are now against the up-estuary-directed subtidal flow there (Figures 3a and 4a). But there are two secondary peaks on the shoals where ebbing currents and down-estuary-directed subtidal flow are working together. While the stress distributions at different tidal phases are similar between moderate and strong down-estuary winds, the stress magnitude is larger during strong wind simply because of the larger wind-driven flow.

[33] The interactions among tides, wind forcing, and gravitational circulations in controlling the stress distribution described above reverse for the up-estuary wind cases. During up-estuary winds, the subtidal axial flow is up estuary on the shoals and down estuary in the channel (Figures 7d and 7e). Therefore, bottom stress peaks in the channel at ebbs when ebbing currents strengthen the down-estuary-directed subtidal flow in the channel (Figures 3d and 4d). Two secondary peaks on the shoals occur at floods as flooding currents and the up-estuary-directed subtidal flow are coherent there (Figures 3f and 4f).

[34] The transport direction of lateral sediment flux is dictated by the near-bottom lateral flows. This is anticipated because the sediment fluxes are larger near the bottom where the suspended sediment concentration is higher.

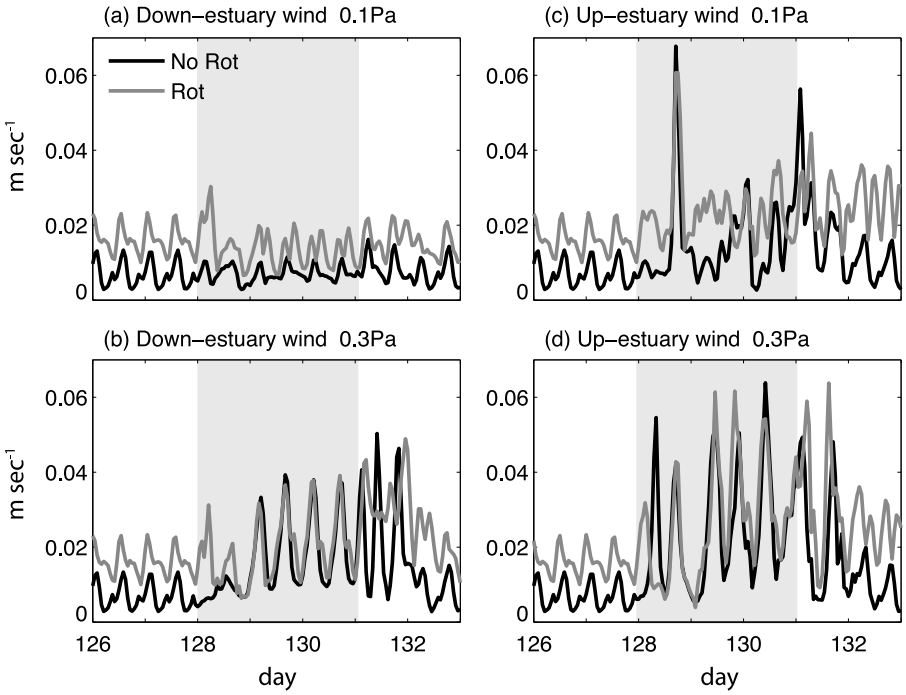

Figure 10. Time series comparisons between lateral flow magnitude ($\bar{v}$ in equation (3)) without rotation (black curves) and with rotation (dark gray curves). The (a) moderate down-estuary wind, (b) strong down-estuary wind, (c) moderate up-estuary wind, and (d) strong down-estuary wind cases are shown. The gray shading represents the event period.

Sediments are transported from channel to shoals during down-estuary winds (Figures 3a–3c and 4a–4c), whereas the transport direction is reversed, becoming from shoals to channel during up-estuary winds (Figures 3d–3f and 4d–4f). Although moderate and strong down-estuary winds both induce channel-to-shoals transport, the near-bottom lateral flows as a transport agent are likely driven by different mechanisms (boundary mixing and differential advection, respectively; section 3) and the sediment fluxes during moderate down-estuary wind are confined close to the bottom due to stratification. The lateral sediment fluxes during strong winds are larger than those during moderate winds because of a combination of larger bottom stress, stronger lateral flows, and weaker stratification. The magnitude of lateral sediment flux also varies within a tidal cycle. In general, the flux magnitude peaks when the bottom stress peaks in the channel (Figures 3c, 3d, 4c, and 4d). Such pattern is due in part to the tidal asymmetry in the strength of bottom stress.

4.2. Depth-Integrated Transport During Events

[35] We assess the net lateral sediment transport (T) by depth-integrating and low-pass filtering the lateral sediment fluxes at the midpoint on the left slope (y = 700 m)

$$T = \left\langle \int_{-h}^{\eta} -v \cdot C \cdot dz \right\rangle, \tag{4}$$

where the angle bracket represents a 33 h low-pass filter, C is the suspended sediment concentration (kg m^{-3}), and v is the lateral flow speed (m s^{-1}). The negative sign in equation (4) is to be consistent with the sign convention in Figure 6. Thus, a positive T means a transport from channel to shoals.

[36] After the transient adjustment, the net lateral sediment transport during the event is toward the shoals/channel during down/up-estuary winds. The magnitude of net transport is as expected to be larger during strong winds (section 4.1). Before the event, the steady state transport driven by boundary mixing [*Chen and Sanford*, 2008] is from channel to shoals with $T = 2.4 \times 10^{-4}$ (kg m^{-1} s^{-1}). During moderate and strong down-estuary wind, this channel-to-shoal transport increases to a maximum value of 3.3×10^{-4} and 3.3×10^{-3}, respectively (Figures 11a and 11b). For both cases, the strongest signal however occurs during the transient adjustment after the event with $T = 4.8 \times 10^{-4}$ and 5.3×10^{-3}. During moderate and strong up-estuary winds, on the other hand, the net transport is from shoals to channel after day 129 with maximum $T = -5.4$ and -8.2×10^{-4}, respectively (Figures 11d and 11e). Note that for strong up-estuary wind, there is a pulse of transport from channel to shoal during the initial transient. This initial pulse is consistent with the positive lateral salinity gradient in Figure 8h. This suggests that, before the lateral salinity gradient is reversed, the salinity in the channel is still higher than that on the shoals, which then drives this transient channel-to-shoal transport. It is also noteworthy that the lateral sediment transport happens in pulses (thin curves in Figure 11). The largest transport occurs at floods/ebbs during down/up-estuary winds after the transient adjustment, as described in section 4.1.

4.3. Influences of Surface Gravity Waves

[37] Including surface gravity waves greatly increases the magnitude of lateral sediment transport. As mentioned in

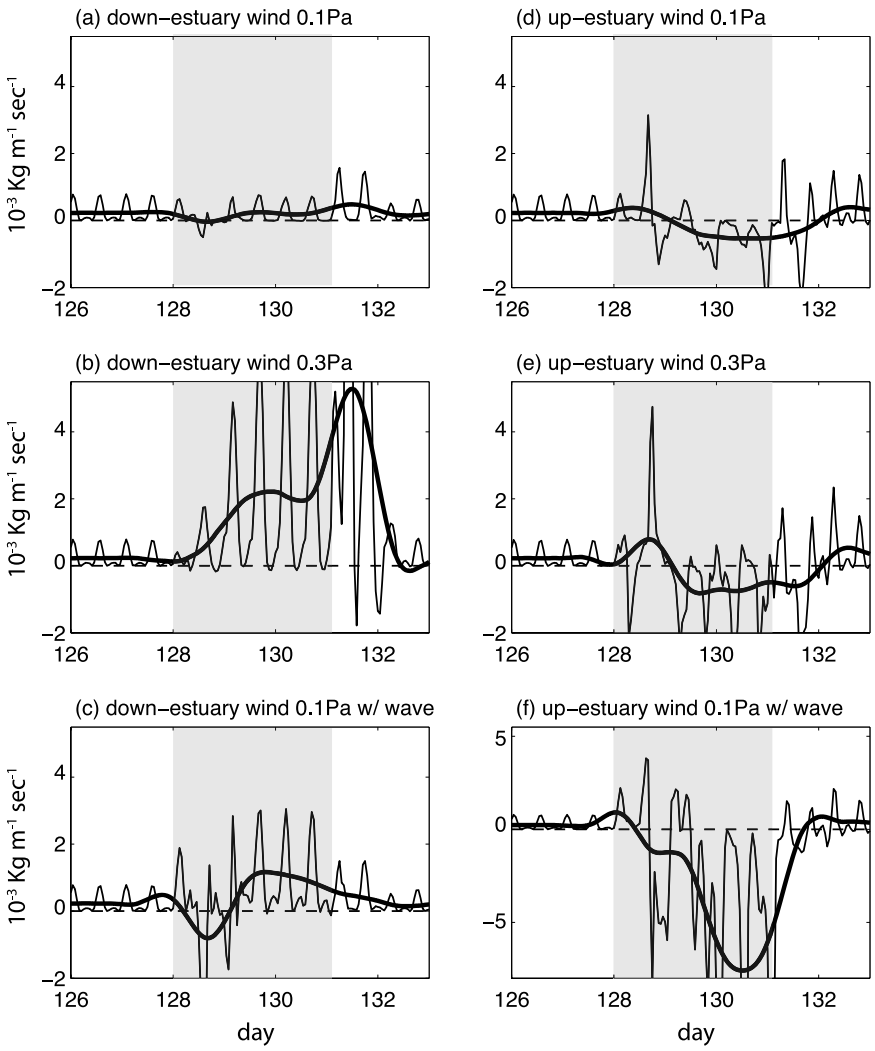

Figure 11. Time series of depth-integrated lateral sediment flux with/without low-pass filtering (thick/thin black curve) (equation (4)). The time series is taken at the midpoint on the left slope. Positive means transport from channel to shoal. (a–c) Down-estuary and (d–f) up-estuary wind cases are shown. Moderate wind (Figures 11a and 11d), strong wind (Figures 11b and 11e), and moderate wind with wind wave forcing (Figures 11c and 11f), respectively. Note that the scale of y axis in Figure 11f is different. The gray shading represents the event period.

the model setup (section 2), two numerical experiments (numbers 15 and 16) accounting for wind-generated waves under moderate winds are carried out to evaluate the influences of surface gravity waves on lateral sediment transport. With waves, the bottom stresses increase strongly toward the shoals during both moderate down- and up-estuary winds, indicating the dominance of wave-induced bottom stresses (solid curves in Figure 12). In the channel, the bottom stresses with waves (solid curves) match those without waves (dashed curves) because the wave orbital velocity has decayed before reaching the channel bottom. High suspended sediment concentration on the shoals is apparent, strongly contrasting with the limited concentration across the entire cross section in the cases without waves (Figures 3c and 3f). The sediment transport direction remains channel to shoal during down-estuary wind and shoal to channel during up-estuary wind, but the magnitude of lateral sediment flux is an order of magnitude larger with waves (Figures 12a, 12b, 3c, and 3f). During moderate up-estuary wind, high suspended sediment concentration reaches the middepth near the channel due to the convergence of sediment fluxes (Figure 12b).

[38] An order of magnitude increase in net transport with waves can be clearly seen from the time series. During moderate down-estuary winds, the net transport increases from 3.3×10^{-4} without waves (Figure 11a) to a maximum value of 1.2×10^{-3} with waves (Figure 11c). During moderate up-estuary winds, on the other hand, the shoal-to-channel transport rate increases from -5.4×10^{-4} without waves (Figure 11d) to a maximum transport of -7.6×10^{-3} with waves (Figure 11f).

5. Discussion and Summary

5.1. Creation of Lateral Salinity Gradient

[39] The cross-sectional structure of salinity, the lateral momentum budget, and the correspondence between $\partial s/\partial y$ and lateral flows suggests that, when the water column is

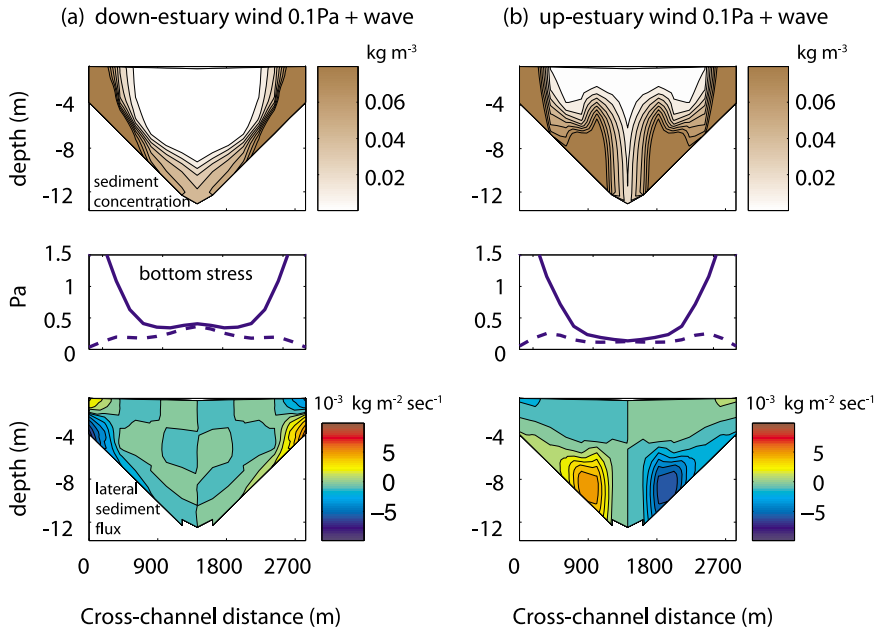

Figure 12. Cross-sectional structures of (top) suspended sediment concentration, (middle) bottom stress, and (bottom) lateral sediment flux for (a) moderate down-estuary wind and (b) moderate up-estuary wind in the presence of wind wave forcing (numbers 15 and 16 in Table 1). Only the profile at maximum flood is shown because the profiles at other tidal phases are qualitatively the same (wave dominated). The solid and dashed curves in Figures 12a and 12b (middle) represent bottom stress distribution with and without wind waves.

largely unstratified, the lateral salinity gradient ($\partial s/\partial y$) is the primary driving force for lateral circulation during axial wind events. The wind modifications of the subtidal axial flow structure and the similar temporal variations between $\partial s/\partial y$ and lateral shear ($\partial u/\partial y$) indicate that lateral shear exerts an important control on $\partial s/\partial y$ through differential advection.

[40] Following *Chen and Sanford* [2008], the governing equation for $\partial s/\partial y$ can be written as

$$\underset{\text{(i)}}{(s_y)_t} = \underset{\text{(ii)}}{-(us_x)_y} - \underbrace{\left[(vs_y)_y + (ws_z)_y\right]}_{\text{(iii)}} + \underbrace{\left[(Ks_z)_z\right]_y}_{\text{(iv)}}, \qquad (5)$$

where s is salinity, (u, v, w) is velocity field, and K is the vertical eddy diffusivity. The first term (i) is the change rate of lateral salinity gradient, the second term (ii) is the differential advection, the third (iii) is a collective term that represents the advection of salt by lateral circulation, and the fourth term (iv) is the lateral variations in vertical mixing. For purely tidally induced differential advection, *Lerczak and Geyer* [2004] simplified the balance to terms (i) and (ii) and found that $\partial s/\partial y$ scaled as $\partial u/\partial y \cdot \partial s/\partial x \cdot 1/\omega$ (ω is the tidal frequency).

[41] We compute all of the terms in equation (5) as for $\partial u/\partial y$ in section 3.2. Each term is low-pass filtered, and we only evaluate nonrotating cases because our focus is on the weakly stratified scenarios in which rotation effect is dynamically less important (section 3.5).

[42] While differential advection (ii) is the dominant forcing term, the scaling by *Lerczak and Geyer* [2004] cannot be applied to our wind-driven cases at subtidal time scale. Taking the strong up-estuary wind case as a representative example, the dominant balance in equation (5) is between differential advection (ii) and advection of salt by lateral circulation (iii) (Figure 13). The differential advection term, as expected, has a similar shape as the lateral shear (Figure 8g), reversing $\partial s/\partial y$ to drive a bottom-convergent lateral circulation. The lateral circulation then advects the salinity field (iii), tending to diminish the existing $\partial s/\partial y$. The development of $\partial s/\partial y$ (i) therefore depends upon a delicate balance of the three terms (ii)–(iv). Nevertheless, this result supports the conclusion that differential advection of the axial salinity gradient by wind-driven, laterally sheared flow is the dominant forcing to create lateral salinity gradients that ultimately drive lateral circulation. At subtidal time scale, the detailed physics that control the variations of $\partial s/\partial y$ appear to be more complex than the simplified two-term balance used by *Lerczak and Geyer* [2004].

5.2. Tidal Variations of the Lateral Salinity Gradient

[43] It can be seen in Figure 5 that the magnitude of the lateral pressure gradient (P_y/ρ_0) is larger during floods under down-estuary winds (2nd vertical line) but is larger during ebbs under up-estuary winds (1st vertical line). Magnitudes of lateral salinity gradient and lateral flow appear to follow the same patterns, especially during strong winds (Figures 6b and 6d). Such tidal variation is likely a result of an additive relationship between wind-induced and tidally induced lateral shear. For example, during strong down-estuary wind, the subtidal lateral shear is positive, meaning that the subtidal axial flow increases (becomes less negative) toward the channel. Flooding currents will further enhance the existing lateral shear whereas ebbing currents will reduce it (Figure 8c), because tidal currents are stronger

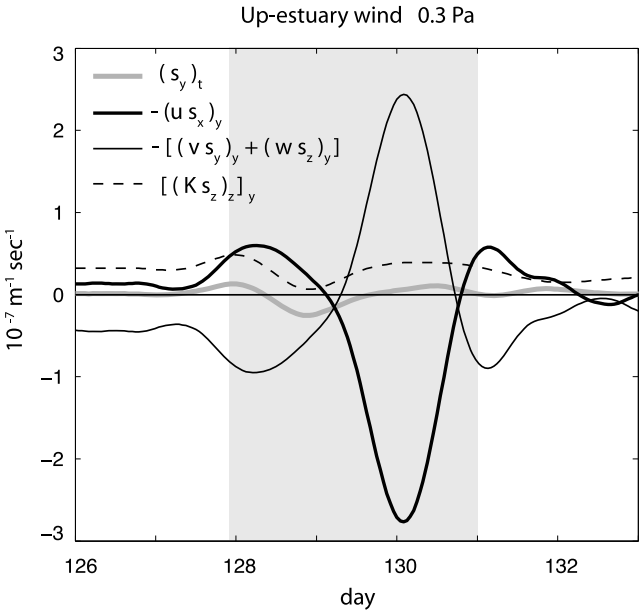

Figure 13. Comparisons of the relative contribution from differential advection (thick black curve), advection of salt by lateral circulation (thin black curve), and lateral variations in vertical mixing (dashed curve) to the change rate of lateral salinity gradient (gray curve) for the strong up-estuary wind case. Each term (equation (5)) is computed in the same way as $\partial s/\partial y$ in Figure 6. The gray shading represents the event period.

in the channel. The enhanced/reduced lateral shear then generates larger/smaller lateral salinity gradient within a tidal cycle. The opposite occurs during strong up-estuary wind when the subtidal lateral shear is negative (Figure 8g). The additive relationship is less clear during moderate winds.

5.3. Driving Mechanism for Lateral Circulation During Axial Winds: A Schematic Diagram

[44] The mechanism of wind-induced differential advection and the resulting lateral circulation can be illustrated by a schematic diagram. Under the simplest condition without wind, tides, and rotation, the subtidal lateral structure of an isohaline is distorted by the density-driven gravitational circulation, forcing high salinity water up estuary in the channel (Figure 14a). Adding axial wind forcing with a stress comparable or larger than the baroclinic pressure gradient force ($|W| \sim or >1$) significantly modifies the lateral structure of subtidal axial flow (e.g., Figure 7). Down-estuary wind tends to enhance the existing lateral shear, whereas up-estuary wind tends to reverse it. The enhancement/reversal of lateral shear advects the axial salinity gradient to create a saltier channel/shoal region during down/up-estuary wind (Figure 14b). The resulting lateral salinity gradient then drives the persistent bottom-divergent/convergent lateral circulation (Figure 14b; also Figures 3d–3f and 4). There are indications that wind-induced and tidally induced lateral shears are largely additive (section 5.2). During down-estuary wind, flooding currents further enhance the lateral shear while ebbing currents reduce it (Figure 14c). The opposite occurs during up-estuary wind. Therefore, a larger lateral salinity gradient occurs when the wind-induced and tidally induced differential advection are in concert, which in turn drives a stronger lateral flow. It should be noted carefully that while differential advection (term (ii) in equation (5)) is shown to be the dominant forcing in section 5.1, the temporal variability of $\partial s/\partial y$ does not depend on differential advection alone. In fact, advection of $\partial s/\partial y$ by lateral circulation itself plays an important role in counterbalancing the creation of $\partial s/\partial y$ by differential advection.

[45] When rotation is included and when the water column is unstratified, the similarities in lateral flow structure, magnitude, and temporal variations between nonrotating and rotating cases suggest that Ekman veering does not drive significant lateral circulation (Figures 9 and 10). The weak rotation (Ekman) effect is most likely due to the weak stratification. When the water column is unstratified, the boundary layers that confine the Ekman transport likely merge and occupy the entire depth. A simple estimate of boundary layer thickness as $\sqrt{2A_v/f}$ (f is the Coriolis parameter; A_v is the cross-sectionally averaged eddy viscosity) yields a value of around 9–10 m which is sufficient to cause the Ekman transport in the surface and bottom layers to merge with each other. The comparable boundary layer thickness and water depth also implies that the time scale for transferring momentum in the vertical is shorter than the rotation time scale ($1/f$) at most of the cross-channel locations. Therefore, the Ekman veering that gives rise to lateral flow is reduced [*Lentz*, 2001].

[46] To sum up the prerequisites, wind-induced differential advection can be an important driving mechanism for lateral circulation during wind events when: (1) $|W| \sim or >1$, which allows axial wind to significantly alter the lateral salinity gradients through laterally sheared advection ((ii) in equation (5)); and (2) the stratification is weak. It should also be noted that this mechanism is only valid after the initial transient response (Figures 6 and 7), which requires an event duration longer than the response time. The response time is controlled by two processes. First is the time required for the wind-driven axial flow (and thus lateral shear) to reach a quasi-steady condition. This time scale is likely associated with the first barotropic seiche mode $T_s = 4l/\sqrt{gH}$ where l is the channel length [*Wang*, 1979; *Chen and Sanford*, 2009]. The other time scale is the time required for lateral shear to modify the preexisting s_y through differential advection ($T_{adv} = s_y/(u_y s_x)$). Given the same s_y, a stronger wind generates a larger lateral shear, leading to a shorter response time. In our cases, T_s and T_{adv} are around 1.6 and 0.6 days, which are shorter than the event duration. Accounting for wind waves is not likely to impact the dominance of wind-induced differential advection because white-capping wind waves enhance vertical mixing that favors the criteria of weak stratification required for effective differential advection. However, the enhanced vertical momentum exchange due to both downward mixing and wave-current interaction in the bottom boundary layer that occurs preferentially on the shallow shoals may limit the magnitude of lateral shear and thus affect the magnitude of lateral flows.

[47] It is worth noticing that the wind controls of lateral density gradient appear to be largely overlooked in the

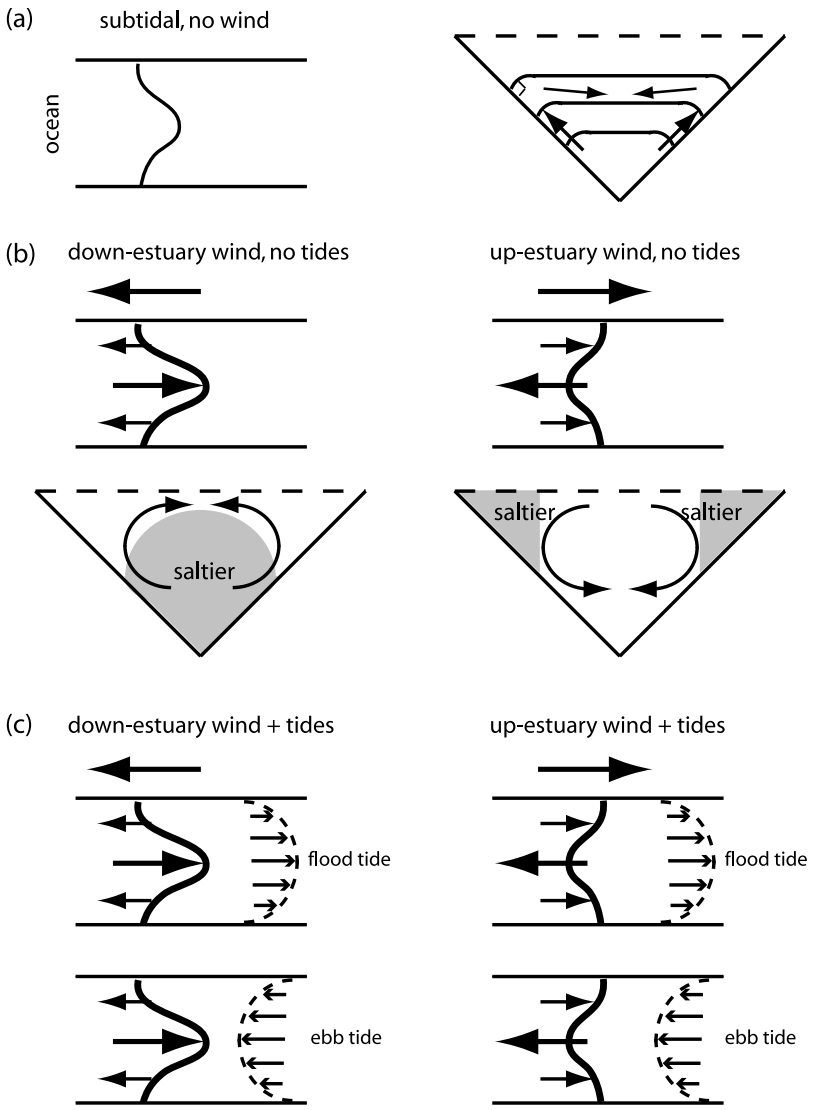

Figure 14. Schematic diagram for the evolution of an isohaline (plan view of a straight channel without rotation) from (a) without wind and tides, (b) adding axial winds, to (c) with wind and tides. The mechanism of wind-induced differential advection is illustrated in Figure 14b, and the additive relationship between wind-induced and tidally induced lateral shear are shown in Figure 14c.

estuarine literature. Its absence in analytical models for lateral circulation [e.g., *Huijts et al.*, 2008] is due to the fact that, to reach a tractable solution, the lateral density gradient is often prescribed and the problem is reduced to 2D. However, our results demonstrate that the lateral density gradient is dynamically linked to axial salt transport by axial wind. In other words, salt and flow fields have to be considered together. The lack of attention from field observations is likely because comprehensive measurement across estuaries is still rare to date. The modeling study here thus serves as an exploration of the topic, and validity of wind-induced differential advection merits further investigations.

5.4. Implications for Sediment Dynamics

[48] Model results in section 4 suggest that sediment transport is from channel to shoal for down-estuary winds but is reversed for up-estuary winds. This pattern can be clearly seen from the event-integrated total transport in Table 2, as the total transport has opposite signs between down- and up-estuary winds. Including wind wave forcing greatly increases the total transport because wind wave action on the shoals leads to a much larger sediment source. The influence of wind waves is particularly strong during up-estuary wind, as shown by the order of magnitude increase in total transport (see also section 4.3).

[49] A consequence of the transport patterns described above is that lateral circulation during up-estuary winds can provide a mechanism to move fine sediments from shoals to channel. The lateral circulation driven by tidally induced differential advection and boundary mixing tends to favor net transport from channel to shoals [*Lerczak and Geyer*, 2004; *Chen and Sanford*, 2008], which cannot explain the net depositional channel region in Chesapeake Bay [*Colman et al.*, 1992]. Transport during up-estuary wind events thus provides a plausible explanation. Additionally, when wind wave forcing is included, frequent up-estuary wind events

Table 2. Lateral Sediment Transport Characteristics for Experiment Numbers 1, 2, 9, 10, 15, 16[a]

		Down-Estuary Wind			Up-Estuary Wind		
	No Wind	0.1 Pa	0.3 Pa	0.1 Pa + Wave	0.1 Pa	0.3 Pa	0.1 Pa + Wave
Total transport	–	76.8	788.5	154.3	−72.3	−101.3	−1038.0
Event-averaged transport rate	2.4	2.2	23.0	4.5	−2.1	−2.9	−30.0

[a]The total transport is the tidally averaged, depth-integrated lateral sediment flux (T in equation (4)) integrated from the event onset to one day after the event ends (day 128–132) to account for the transient effects. The event-averaged transport rate is the total transport divided by the period of time integral (4 days here). The units of the total transport and the event-averaged transport rate are kg m^{-1} and 10^{-4} kg m^{-1} s^{-1}, respectively. Here positive means from channel to shoal.

are not required to result in a net depositional channel. The total transport after a 3 day up-estuary wind event needs about 50 days of background channel-to-shoal transport to compensate (Table 2). This result highlights the importance of resolving episodic events with wind wave coupling, which merits further investigation. Finally, transient effects during the adjustment period can be important. While the instantaneous sediment fluxes are stronger during stronger wind stresses (Figure 11), the total transport may not show the same trend. For example, the total transport during strong up-estuary wind is only slightly higher than moderate up-estuary wind (Table 2). This is due to the initial pulse of channel-to-shoal transport during the transient adjustment (Figure 11e; day 128–129.5). This also implies that limited sediment supply [e.g., *Sanford*, 2008], as opposed to an unlimited supply here, may further complicate sediment transport patterns during wind events. A more realistic sediment bed model is thus needed for future investigations on event-driven transport.

[50] **Acknowledgments.** We thank the ROMS code developer/user community and the financial support from ONR through the Community Sediment Transport Modeling (CSTM) project. Helpful comments from two anonymous reviewers, Carl Friedrichs and Elizabeth North, are appreciated. This is UMCES publication 4343.

References

Canuto, V. M., et al. (2001), Ocean turbulence. Part I: One-point closure model—Momentum and heat vertical diffusivities, *J. Phys. Oceanogr.*, *31*, 1413–1426, doi:10.1175/1520-0485(2001)031<1413:OTPIOP>2.0.CO;2.

Chant, R. J., and E. Wilson (1997), Secondary circulation in a highly stratified estuary, *J. Geophys. Res.*, *102*, 23,207–23,216, doi:10.1029/97JC00685.

Chen, S.-N., and L. P. Sanford (2008), Lateral circulation driven by boundary mixing and the associated transport of sediments in idealized partially mixed estuaries, *Cont. Shelf Res.*, *29*, 101–118, doi:10.1016/j.csr.2008.1001.1001.

Chen, S.-N., and L. P. Sanford (2009), Axial wind effects on salinity structure and longitudinal salt transport in idealized, partially mixed estuaries, *J. Phys. Oceanogr.*, *39*, 1905–1920, doi:10.1175/2009JPO4016.1.

Colman, S. M., J. P. Halka, and C. H. Hobbs III (1992), Patterns and rates of sedimentation in the Chesapeake Bay during the Holocene Rise in sea level, in *Patterns and Rates of Sedimentation in Chesapeake Bay During the Holocene Rise in Sea Level*, edited by C. Fletcher and J. F. Wehmiller, pp. 101–111, Soc. for Sediment. Geol., Tulsa, Okla.

Csanady, G. T. (1973), Wind-induced barotropic motions in long lakes, *J. Phys. Oceanogr.*, *3*, 429–438, doi:10.1175/1520-0485(1973)003<0429:WIBMIL>2.0.CO;2.

Dean, R. G., and R. A. Dalrymple (1991), *Water Wave Mechanics for Engineers and Scientists*, World Sci, Singapore.

Fischer, H. B., et al. (1979), *Mixing in Inland and Coastal Waters*, Academic, New York.

Fugate, D. C., et al. (2007), Lateral dynamics and associated transport of sediments in the upper reaches of a partially mixed estuary, Chesapeake Bay, USA, *Cont. Shelf Res.*, *27*, 679–698, doi:10.1016/j.csr.2006.11.012.

Geyer, W. R. (1997), Influence of wind on dynamics and flushing of shallow estuaries, *Estuarine Coastal Shelf Sci.*, *44*, 713–722, doi:10.1006/ecss.1996.0140.

Geyer, W. R., et al. (1998), Lateral trapping of sediment in a partially mixed estuary, in *Physics of Estuaries and Coastal Seas*, edited by J. Dronkers and M. Scheffers, pp. 115–124, A. A. Balkema, Brookfield, Vt.

Goda, Y. (2003), Revisiting Wilson's formulas for simplified wind-wave prediction, *J. Waterw. Port Coastal Ocean Eng.*, *129*, 93–95, doi:10.1061/(ASCE)0733-950X(2003)129:2(93).

Guo, X., and A. Valle-Levinson (2008), Wind effects on the lateral structure of density-driven circulation in Chesapeake Bay, *Cont. Shelf Res.*, *28*, 2450–2471, doi:10.1016/j.csr.2008.06.008.

Haidvogel, D. B., et al. (2000), Model evaluation experiments in the North Atlantic basin: Simulations in nonlinear terrain-following coordinates, *Dyn. Atmos. Oceans*, *32*, 239–281, doi:10.1016/S0377-0265(00)00049-X.

Hansen, D. V., and M. Rattray (1965), Gravitational circulation in straits and estuaries, *J. Mar. Res.*, *23*, 104–122.

Huijts, K. M. H., et al. (2006), Lateral entrapment of sediment in tidal estuaries: An idealized model study, *J. Geophys. Res.*, *111*, C12016, doi:10.1029/2006JC003615.

Huijts, K. M. H., et al. (2008), Analytical study of the transverse distribution of along-channel and transverse residual flows in tidal estuaries, *Cont. Shelf Res.*, *29*, 89–100, doi:10.1016/j.csr.2007.1009.1007.

Jones, W. P., and B. E. Launder (1972), The prediction of laminarization with a two-equation model of turbulence, *Int. J. Heat Mass Transfer*, *15*, 301–314, doi:10.1016/0017-9310(72)90076-2.

Kerhin, R., et al. (1988), The surficial sediments of Chesapeake Bay, Maryland: Physical characteristics and sediment budget, investigation report, 43 pp., Md. Geol. Surv., Baltimore, Md.

Lacy, J. R., and S. G. Monismith (2001), Secondary currents in a curved, stratified, estuarine channel, *J. Geophys. Res.*, *106*, 31,283–31,302, doi:10.1029/2000JC000606.

Langland, M., and T. M. Cronin (2003), A summary report of sediment processes in Chesapeake Bay and watershed, *Water Resour. Invest. Rep. 03-4123*, U.S. Geol. Surv., New Cumberland, Pa.

Large, W. G., and S. Pond (1981), Open ocean momentum flux measurements in moderate to strong winds, *J. Phys. Oceanogr.*, *11*, 324–336, doi:10.1175/1520-0485(1981)011<0324:OOMFMI>2.0.CO;2.

Lentz, S. J. (2001), The influence of stratification on the wind-driven cross-shelf circulation over the North Carolina shelf, *J. Phys. Oceanogr.*, *31*, 2749–2760, doi:10.1175/1520-0485(2001)031<2749:TIOSOT>2.0.CO;2.

Lerczak, J. A., and W. R. Geyer (2004), Modeling the lateral circulation in straight, stratified estuaries, *J. Phys. Oceanogr.*, *34*, 1410–1428.

Li, M., et al. (2005), Simulations of Chesapeake Bay estuary: Sensitivity to turbulence mixing parameterizations and comparison with observations, *J. Geophys. Res.*, *110*, C12004, doi:10.1029/2004JC002585.

Lin, W., et al. (2002), Wave measurement and modeling in Chesapeake Bay, *Cont. Shelf Res.*, *22*, 2673–2686, doi:10.1016/S0278-4343(02)00120-6.

Madsen, O. S. (1994), Spectral wave-current bottom boundary layer flows, paper presented at 24th International Conference on Coastal Engineering, Am. Soc. of Civ. Eng., Kobe, Japan.

Monismith, S. G. (1986), An experimental study of the upwelling response of stratified reservoirs to surface shear stress, *J. Fluid Mech.*, *171*, 407–439, doi:10.1017/S0022112086001507.

Nunes, R. A., and J. H. Simpson (1985), Axial convergence in a well-mixed estuary, *Estuarine Coastal Shelf Sci.*, *20*, 637–649, doi:10.1016/0272-7714(85)90112-X.

Ott, M. W., and C. Garrett (1998), Frictional estuarine flow in Juan de Fuca Strait with implications for secondary circulation, *J. Geophys. Res.*, *103*, 15,657–15,666, doi:10.1029/98JC00019.

Resio, D., et al. (2002), *Meteorology and Wave Climate*, U.S. Army Corps of Eng., Washington, D. C.

Sanay, R., and A. Valle-Levinson (2005), Wind-induced circulation in semienclosed homogeneous, rotating basins, *J. Phys. Oceanogr.*, *35*, 2520–2531, doi:10.1175/JPO2831.1.

Sanford, L. P. (2008), Modeling a dynamically varying mixed sediment bed with erosion, deposition, bioturbation, consolidation, and armoring, *Comput. Geosci.*, *34*(10), 1263–1283, doi:10.1016/j.cageo.2008.02.011.

Sanford, L. P., et al. (1990), Covariability of dissolved oxygen with physical processes in the summertime Chesapeake Bay, *J. Mar. Res.*, *48*, 567–590.

Scully, M. E., et al. (2005), Control of estuarine stratification and mixing by wind-induced straining of the estuarine density field, *Estuaries*, *28*, 321–326, doi:10.1007/BF02693915.

Scully, M. E., et al. (2009), The influence of lateral advection on the residual estuarine circulation: A numerical modeling study of the Hudson River Estuary, *J. Phys. Oceanogr.*, *39*, 107–124.

Valle-Levinson, A., et al. (2000), Convergence of lateral flow along a coastal plain estuary, *J. Geophys. Res.*, *105*, 17,045–17,061, doi:10.1029/2000JC900025.

Wang, D.-P. (1979), Wind-driven circulation in the Chesapeake Bay, winter 1975, *J. Phys. Oceanogr.*, *9*, 564–572, doi:10.1175/1520-0485(1979)009<0564:WDCITC>2.0.CO;2.

Warner, J. C., et al. (2005), Numerical modeling of an estuary: A comprehensive skill assessment, *J. Geophys. Res.*, *110*, C05001, doi:10.1029/2004JC002691.

Winant, C. D. (2004), Three-dimensional wind-driven flow in an elongated, rotating basin, *J. Phys. Oceanogr.*, *34*, 462–476, doi:10.1175/1520-0485(2004)034<0462:TWFIAE>2.0.CO;2.

Wong, K. C. (1994), On the nature of transverse variability in a coastal plain estuary, *J. Geophys. Res.*, *99*, 14,209–214,222, doi:10.1029/94JC00861.

Zhong, L., and M. Li (2006), Tidal energy fluxes and dissipation in the Chesapeake Bay, *Cont. Shelf Res.*, *26*, 752–770, doi:10.1016/j.csr.2006.02.006.

S.-N. Chen, Applied Ocean Physics and Engineering Department, Woods Hole Oceanographic Institution, Mail Stop 10, Woods Hole, MA 02543, USA. (schen@whoi.edu)

D. K. Ralston, Applied Ocean Physics and Engineering Department, Woods Hole Oceanographic Institution, Mail Stop 11, Woods Hole, MA 02543, USA.

L. P. Sanford, Horn Point Laboratory, University of Maryland Center for Environmental Science, 2020 Horns Point Rd., PO Box 775, Cambridge, MD 21613, USA.